

# Three-Dimension Dithering and its effect on the Interfacial Strength of Multi-Material and Emulated Multi-Material Additive Manufacturing Processes

James D. Willmott<sup>a</sup>, Richard J. Bibb<sup>a</sup>, Andrew A. Johnson<sup>a</sup>, Abby M. Paterson<sup>a</sup>

<sup>a</sup>*School of Design and Creative Arts, Loughborough University, Loughborough, LE11 3TU, UK*

---

## Abstract

Multi-Material Additive Manufacturing (MMAM) offers the potential for superior functional parts by varying properties throughout a structure. Previous work has shown that the interface region of such MMAM parts has great importance on their overall strength. Most of these studies have focused on rigid-compliant interfaces within parts manufactured via material jetting (MJT). This work focuses, initially, on the creation of different interfacial geometries within functionally graded tensile bars by extending two dimensional dithering algorithms from the realm of image processing into the third dimension. It tests these dithered patterns, along with Schwarz P and Gyroid structures, across rigid-compliant MJT interfaces before further exploring the previously unaddressed question of how these different geometries affect interfacial strength across rigid-rigid interfaces for both UV cured materials, via MJT, and thermoplastic materials, via a new prototype electrophotographic toner-based AM system. Within the MJT parts, the samples often failed inside the large regions of the more compliant material rather than at the interface itself. In addition, the interfacial length is shown to have more effect on the mechanical properties compared to interface pattern. However, the thermoplastic samples consistently failed within the interface region. The toughness of these thermoplastic parts increased with an increase in the connected surface area in the tensile direction between the largest regions of each of the two materials, with three dimensional random dithering over a 20 mm gradient length exhibiting the toughest interface overall (40.8% increase in the work at break when compared to a control sample with no special interfacial geometry). This work, therefore, provides a new emphasis to explore, within the context of the design of thermoplastic multi-material interfaces, geometries that increase this connected surface area.

*Keywords:*

Multi-Material, Interfaces, PolyJet, STEP, Dithering

---

## 1. Introduction

Multi-Material Additive Manufacturing (MMAM) has enabled the creation of end-use functional parts in a variety of industries, including medical [1, 2], electronics [3] and soft robotics [4]. The advantage of using MMAM for these applications is that part consolidation can be achieved with variable material properties throughout the structure, utilising the beneficial properties of each material whilst minimising detrimental ones. In terms of polymer systems, one of the most common commercial MMAM processes is material jetting (MJT), where designers can take advantage of the fine spatial resolution, voxel-level control and relatively wide selection of material properties to create objects with enhanced performance, applicable for a large variety of products. Several studies have investigated the interfacial strength of samples produced via one such MJT process, namely PolyJet (Stratasys Ltd., USA). These studies typically investigate the interface between a rigid and a compliant material, and have shown effects on different scales. On the micro-scale, researchers have characterised the local property variation and material mixing over a planar interface, showing these variations depend upon the printing orientation (i.e. inter-layer vs intra-layer interfaces or whether or not material mixing occurs before the material is cured via Ultra-Violet (UV) light)[5, 6] and take a hyperbolic tangent or sigmoid shape [5, 7, 8]. On the macro-scale, differences in interfacial strength have been reported, based on the stiffness of the more compliant material [9], the addition of intermediate layers between the rigid-compliant interface [6, 10], and different geometric interfacial patterns [11, 12, 13].

This work looked to investigate two areas of comparison that have thus far been missing from such studies. Firstly, within a MJT context, the effect of the pattern itself on the interfacial strength, by comparing the same interfacial patterns across a rigid-rigid interface as well as a rigid-compliant one. Secondly, since the mechanical properties of MJT parts are in general not suitable for end use structural parts [14]; parts can become more brittle over time [15]; and there are skin irritants and sensitizers present in MJT resins [16] that might cause health concerns especially if uncured resin made it into a product, several polymer applications use thermoplastic materials. This work, therefore, also investigated a new electrophotographic MMAM process using thermoplastic toner materials with a similar resolution to PolyJet to assess if the trends seen in interfacial strength are comparable across different processes.

### 1.1. Dithering

This paper also expands upon the concept of three different Three-Dimensional (3D) dithering techniques, stemming from Two-Dimensional (2D) equivalents in the world of image processing: Random dithering, Dispersed-Dot Ordered (or Bayer) dithering [17] and Error Diffusion dithering [18]. Dithering is a process, with a number of different techniques, that is typically used in 2D image processing to enable better representation of images using a much smaller palette. One of the most common applications of dithering is to convert smooth greyscale to black and white as can be seen in Figure 1.



Figure 1: Image showing the different 2D dithering algorithms. Top Left = Original Image, Top Right = Random dithering, Bottom Left = Bayer dithering, Bottom Right = Error Diffusion dithering.

Many modern MMAM hardware solutions, including the two processes used in this study, are capable of using image or bitmap stacks, with each layer represented by a 2D image, in order to have full control over the material distribution throughout an object. This leads to a voxel representation when these stacks are combined. Images within stacks exported from Computer Aided Design (CAD) packages can have a bit depth of 8 and therefore over 16 million different possible RGB (Red/Green/Blue) colour combinations. These combinations could be used to represent a colour itself, but could also be used to represent other aspects, such as process parameter changes or, like in the context of this work, different material properties. Whilst CAD packages can handle smooth transitions and millions of possibilities for colour, most MMAM approaches can only deposit one material per voxel and are limited to

only a few materials in total. The principles of dithering to reduce palette size to only a few printable colours or materials are therefore very applicable to this work methodology and have been theorised for a relatively long time. In 2003, Cho et al. stated the need for dithering approaches to be three-dimensional in order to avoid what they described as ‘vertical streaks’ or columns of material [19]. This is relevant as applying Bayer or Error Diffusion dithering to a stack of identical 2D input greyscale images, like those representing a functionally graded material along one axis, would lead to each output layer of the dithered image stack also being identical. This effect is visualised in Figure 2.

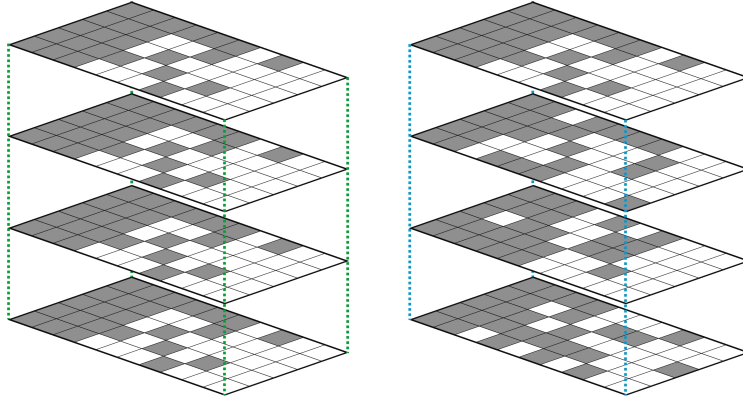


Figure 2: Identical output layers lead to columns or vertical streaks (Left). If each output layer is different to those above and below it, then no columns would be observed (Right).

Within the context of MMAM, several researchers have theorised and printed dithered patterns and interfaces, although not all have used this terminology. After Cho’s initial discussion on the concept, little work was carried out in the following decade, possibly due to limitations in the hardware to deposit multiple materials on the voxel level. However, more recently, a number of research groups have begun to investigate the possibilities dithering enables, largely supported by PolyJet printing coupled with GrabCAD Print’s VoxelPrint functionality (Stratasys Ltd., USA). The most common approach in these studies has been Random 3D dithering; this methodology minimises the vertical streaking described above since each layer has a different output, even if each input image is identical. Several different researchers have all described assigning material based upon thresholding using random probabilities, which describes the process of a Random dither without using this name [11, 20, 21]. These studies showed that this approach to material distribution is not only feasible for creating functional graded samples but also that the interface showed greater toughness than some common Triply Periodic Minimal Surface (TPMS) structures

due to the ability of individual or groups of voxels to halt crack propagation [22]. The disadvantages of this methodology are that, on the micro scale, properties can vary significantly based on the random distribution and visually parts look less smooth in their transitions from regions of one colour or material to another.

Separate research groups have applied a different dithering approach to MMAM, having implemented material distribution via an Error Diffusion dithering algorithm. These Error Diffusion algorithms, explained further in Section 2.4.1, loop through the pixels in an image, thresholding based upon a typically fixed value and outputting a new value for that pixel from the smaller palette. The error between the output value and original value can then be calculated, split according to pre-determined kernels, and ultimately propagated to the surrounding pixels to ensure smooth transitions. One of the groups investigated the effect of voxel size [23], and fatigue [24, 25] on digital and functionally graded MMAM parts. However, there is no mention of applying this algorithm in 3D in their work and as such it is assumed that the dither is a 2D one. Since 2D Error Diffusion algorithms give the same solution for the same input each time, this methodology suffers from vertical streaks but has the advantage of smoother gradients and more individual voxels, increasing the total surface area between materials. One prior example of an Error Diffusion algorithm being propagated into 3D for use in additive manufacturing (AM), comes from work developing a MMAM specific library for Python called VoxelFuse [12, 26]. This work implements one such pre-determined kernel, known as a Stucki filter [27] extended to three dimensions, as seen in Figure 3, and found that PolyJet printed dogbones containing a 3D dithered pattern outperformed a 2D equivalent dither along with several TPMS and lattice structures in terms of ultimate tensile stress (UTS) [12].

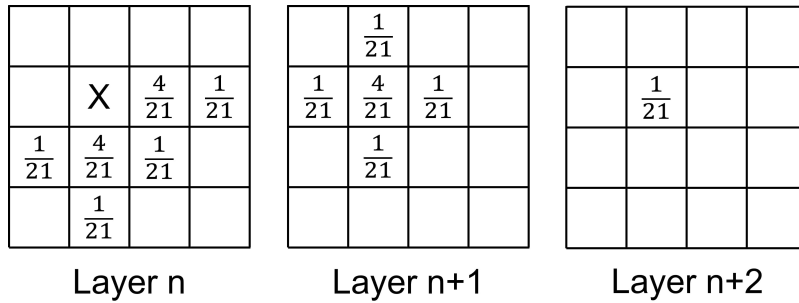


Figure 3: Stucki Filter adapted to 3D showing the fraction of the error is passed to each of the surrounding voxels, where X = current voxel being analysed. Image recreated from [12] with permission.

### 1.2. Electrophotography as an AM Process

Electrophotography (EP), or Xerography, is a process that originated in 2D copying and printing whereby ink in the form of a dry toner powder is selectively deposited onto a substrate, typically paper, via a photoconductive roller. The process contains six main steps:

1. **Charging** – A uniform negative charge is applied to the photoconductor.
2. **Exposure** – A light source, usually a laser or LED array, selectively discharges the photoconductor, creating a field that represents the image or the ‘latent image’.
3. **Developing** – Toner particles are attracted to the photoconductor due to the potential difference between the hopper, where the toner is stored, and the latent image. This forms a real image of toner particles on the photoconductor.
4. **Transfer** – The image is transferred from the photoconductor onto the substrate, using opposite electrostatic forces and an additional roller. This process step requires the linear speed of the substrate to match the rotational speed of the drum [28] and can be direct or via an intermediate belt or roller.
5. **Fusing** – The toner image is fused using heat and pressure, typically using a pair of heated rollers. In 2D, this is fusing it to the substrate but in 3D it is fused to the already deposited material.
6. **Cleaning** – Undeposited toner is removed physically using a blade (or equivalent) and the underlying latent image is erased by exposing the photoconductor to a uniform light source.

Since the EP process for 2D printing has been well developed since its origins in the 1930s [29], the idea to utilise this approach for AM is not a novel one; the first patent describing an EP 3D printer was granted in 1992 [30]. Since then, several attempts have been made to develop a working machine [31, 32, 33, 34, 35, 36]. In general, the approach has been to deposit layers of material (or, more recently, materials) using the 6-step process described above, either directly onto a build plate which lowers or with an intermediate transfer onto a belt, followed by a fusing of layers using heat and/or pressure. This therefore makes AM using EP fundamentally a sheet lamination process. The advantages of EP as an AM process are numerous. Theoretically any material that can be converted into a suitable toner can be printed, enabling the manufacture of a wide range of engineering materials. These materials can also be deposited at very fine resolutions, making use of the decades of developments of EP engines for 2D printers where resolutions of 600, 1200 or even 2400 dpi are now readily available commercially [37]. In addition, there is the possibility of combining multiple EP engines together each with a different material in

order to manufacture MMAM components, in the same way that four engines in a CMYK (Cyan/Magenta/Yellow/Black) 2D EP printer enable full colour reproduction. Finally, EP as a process also offers a significant speed advantage over other thermoplastic MMAM processes, such as material extrusion, since entire layers can be deposited simultaneously. However, groups working on EP for AM have come across two major challenges: Limitations in the height of parts and issues with registration, both of multiple materials within a singular layer as well as complete layers on top of one another. The ability to create parts greater than 100 layers has proved to be a major obstacle, especially when trying to deposit directly from the EP engine onto the build plate as the previous deposited material insulates the electrostatic forces required to transfer toner from the roller to the substrate [33, 34]. Benning and Dalgarno demonstrated major improvements in the number of layers, printing objects of up to 700 layers using a custom printer with a transfer belt and a heated roller to combine layers onto a card build platen with no electrostatic field present in this consolidation region [36]. These samples, however, although much greater in Z height, still contained deposition issues, particularly at the trailing edge. The issue of registration has, thus far, not been improved upon in literature, however one machine manufacturer, Evolve Additive Solutions, a spinout from Stratasys, has been able to minimise the issue by implementing a closed feedback loop into their proprietary printing process, which they term Selective Thermoplastic Electrophotographic Process or STEP for short. A representation of this system with two EP engines (for two different materials) and a sensor for the registration of layers is shown in Figure 4.

### *1.3. Summary*

As discussed in Section 1.1, 3D dithering presents a method to potentially increase the interfacial strength of MMAM parts. Whilst some researchers have looked at the topic, there is scope to include more patterns and material combinations within one combined study. In addition, Electrophotographic AM methods (Section 1.2) exhibit great promise to produce multi-material parts from engineering grade polymers but work is required to more thoroughly explore the capabilities of these printers within a MMAM context. This study will build on these two topics to create a more well-rounded understanding of the interfacial strength within polymer MMAM parts.

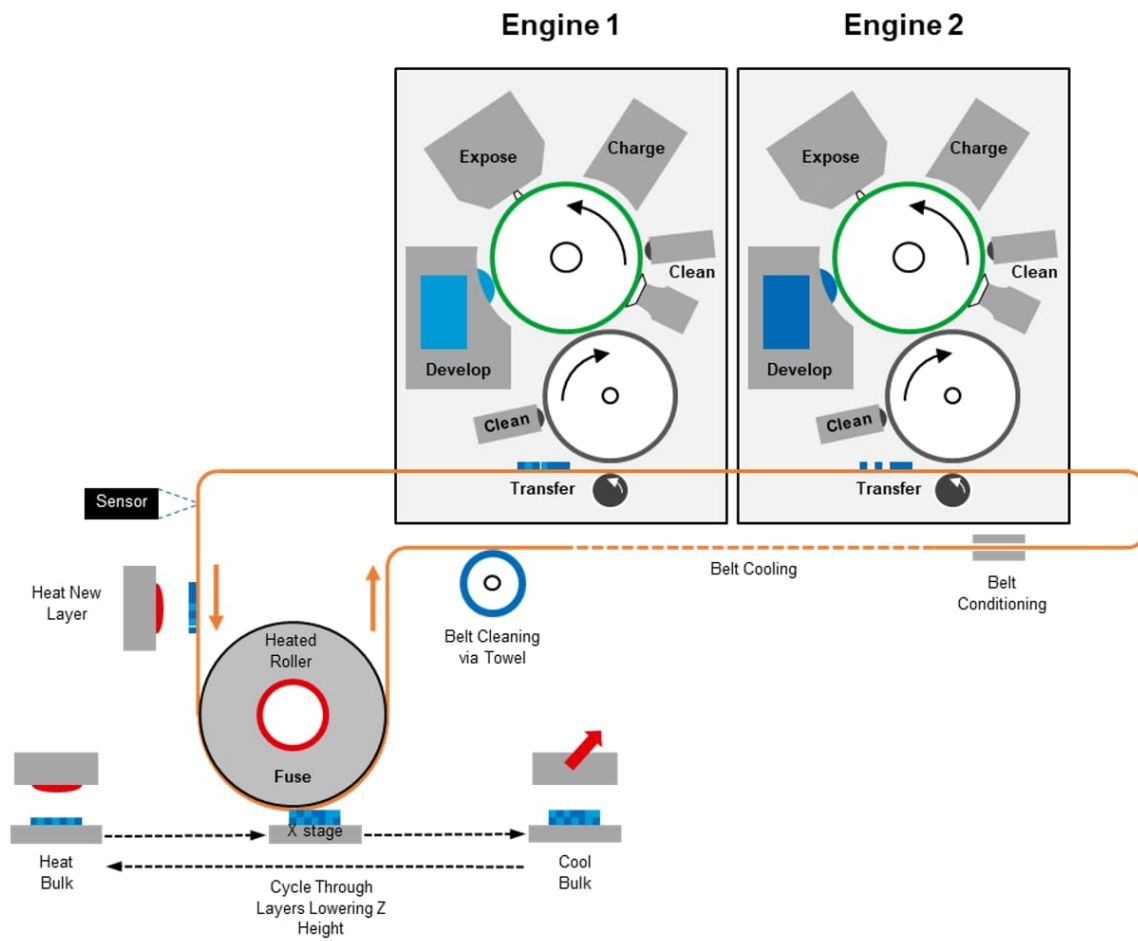


Figure 4: STEP Process Diagram. Text in **bold** indicates the six fundamental EP process steps.

## 2. Materials and Methods

### 2.1. AM Printers / Processes

Two different MMAM-enabled printers were used in this study. The first was a prototype machine produced by the aforementioned Evolve Additive Solutions, manufacturing parts using their proprietary STEP technology. This process can be considered as sheet lamination where multiple EP engines deposit a single multi-material layer of toner onto a transfer belt which are subsequently stacked and fused between a heated roller and moving platen. The second was a PolyJet printer, the Stratasys J826 Prime, which uses a material jetting process to deposit material. Differences in both in-plane XY resolution and layer heights exist between these two printing technologies, with this information summarised in Table 1.

Table 1: Comparison of the two systems used in this study.

Printing Technology	Resolution <sub>x</sub> (DPI)	Resolution <sub>y</sub> (DPI)	Layer Height ( $\mu\text{m}$ )
Stratasys J826 Prime	600	300	27
Evolve STEP Prototype	600	600	16

Since this difference exists between the two technologies, for this work it was decided to create voxels of similar dimensions by using 300 DPI resolution in both X and Y directions and with a single layer in PolyJet and two layers in STEP. This means that the final voxel size was 85 x 85 x 27  $\mu\text{m}$  for PolyJet and 85 x 85 x 32  $\mu\text{m}$  for STEP. In order to create samples with material compositions that vary at the voxel level, MATLAB code (The MathWorks Inc., USA) was used to import, modify and export PNG stacks. For the prototype STEP machine, the required inputs were two 1-bit depth images per layer, with each image relating to one of the electrophotographic engines showing where material from that engine should be deposited. However, for the layers to be interpreted by the Stratasys machine, a colour PNG image is required with up to seven distinct RGB values (one for each material loaded into the machine) plus an eighth value for the background where no material would be deposited. A further step of converting these colour PNGs into a printable .gcvf format was required using the VoxelPrint add-on to the GrabCAD slicer (Stratasys Ltd., USA).

### 2.2. Materials

The PolyJet experiments used two different combinations of materials. These were a rigid-compliant pairing [Vero Pure White (VW) and Agilus30 Black (AB)

(Stratasys Ltd., USA)] as well as a rigid-rigid combination [VW and Vero Pure Black (VB)]. These MJT materials were chosen due to being the most used rigid and compliant materials respectively and being the materials available with the most similar properties on the J826 Prime system to those of previous studies referenced in Section 1. On the other hand, only one material (ABS) (Evolve Additive Solutions, USA) was able to be used for the STEP related experiments. This was primarily due to a shortage of suitable, printable materials being available on account of the lack of maturity of this particular MMAM process and the prototype STEP machine only containing two usable EP engines, one for support material and the other for one part material. Further discussion on how this was used to emulate MMAM is described in Section 2.4.3. The tensile properties of Young’s Modulus (E), UTS, and Elongation at Break ( $\epsilon_B$ ), as stated on respective data sheets [38, 39, 40], for each of the materials used are given in Table 2.

Table 2: Tensile properties of the materials used in this study as stated on respective data sheets [38, 39, 40]. No value of E is stated on the data sheet for AB due to its elastomeric response.

Material	Printing Technology	E (MPa)	UTS (MPa)	$\epsilon_B$ (%)
VW	PolyJet	2000 - 3000	50 - 65	10 - 25
VB	PolyJet	2000 - 3000	50 - 65	10 - 25
AB	PolyJet	N/A	2.4 – 3.1	220 – 270
ABS	STEP	1770	37	15

### 2.3. Tensile Testing and Analysis

The testing procedure followed was in accordance with ISO 527-2019 [41], with the 1BA sample selected for its size, the dimensions of which are shown in Figure 5. The gauge width and thickness were measured using a micrometer for every sample. A ZwickRoell Z005 Multi-tester with a multi extensometer (ZwickRoell, Denmark) was used for the testing with a 5kN Class 05 load cell attached. The cross-head displacement rate was 1 mm/min initially, to determine the Young’s Modulus of the material, followed by 100 mm/min thereafter. Values for E, UTS,  $\epsilon_B$  and Work at break ( $W_B$ ) were calculated from the Force – Extension data.

### 2.4. Creation of Tensile Samples

#### 2.4.1. Interfacial Patterns

Six interfacial patterns were proposed as part of this study, along with three different lengths of gradient. These were compiled into a full factorial Design of

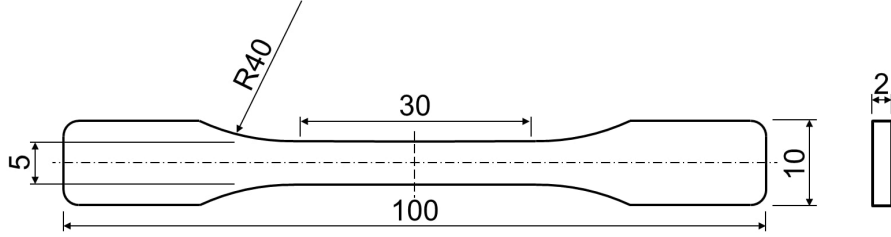


Figure 5: ISO 527 - 1BA sample used in this study. Units are stated in mm.

Experiments with three additional designs printed and tested for each of the three material / printer combinations: solid samples of each of the two base materials and a final design with a planar interface (**PI**), i.e. no transition region. Five samples of each design were printed giving a total number of samples of 105 for each material / printer combination and 315 overall.

Table 3: Interfacial Patterns and Lengths used in the DoE study.

Interfacial Patterns	Gradient Lengths (mm)
Schwarz P TPMS – <b>SP</b>	2, 10, 20
Gyroid TPMS – <b>GY</b>	2, 10, 20
Random Dither in 2D (XY Plane Only) – <b>R2</b>	2, 10, 20
Random Dither in 3D – <b>R3</b>	2, 10, 20
Error Diffusion Dither in 3D – <b>E3</b>	2, 10, 20
Ordered Dither in 3D – <b>O3</b>	2, 10, 20

In order to create the TPMS patterns (i.e. GY and SP) with unit cell volume of 1 x 1 x 1 mm, Volumetric Modelling capabilities within Autodesk Fusion 360 (Autodesk Inc., USA) were used on a CAD file of the ISO 527 - 1BA dog bone specimen. This involved creating a gradient in thickness of the TPMS structure across the centre section of the sample with the lengths given in Table 3. The dithered samples (i.e. R2, R3, E3, and O3) were created in an identical methodology except the colour channel was varied to create a gradient from red to black rather than the unit cell thickness. The Autodesk files containing GY, SP and colour gradients for 20 mm gradient length can be seen in Figure 6. Each of these were then exported from within the Volumetric Modelling tool, with resolutions in dots per inch (DPI) equal to that of the voxel size decided previously, i.e. 300 x 300 x 941 DPI for PolyJet and 300 x 300 x 794 DPI for STEP. The different dithering patterns were applied to the coloured export image stack via MATLAB functions described briefly here.

The pseudo code for these algorithms can be found in the supplementary document (Algorithms 1, 2, and 3 respectively).

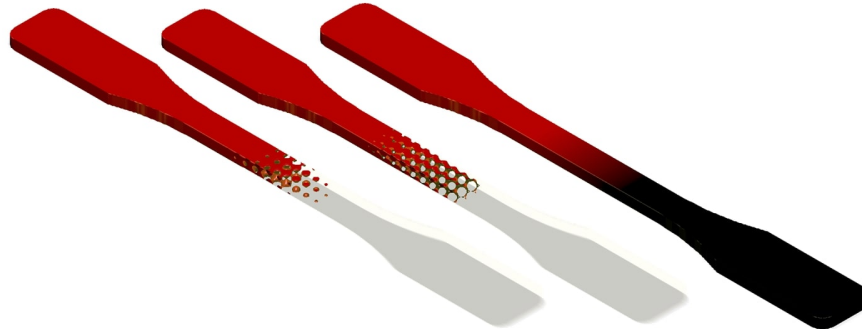


Figure 6: Dogbone samples with 20 mm gradients generated using Volumetric Modeling capabilities. Left = SP , Center = GY, Right = Colour.

### Random Dither

The 8 bit-depth input PNG stack was loaded, and the red colour channel was extracted to leaving greyscale images containing values between 0 and 255. After this, the algorithm looped through the pixels in each row, column and layer in turn creating a random threshold value for each. It then compared the value of the original image stack to this threshold. If the value in the original was greater, then the output was 1, representing the first material. If it was less than the threshold, then the output was 0 which is analogous to the second material. For the R2 pattern, only a single image was inputted with the output subsequently duplicated for all layers to create a pattern with the columnated effect described previously.

### Error Diffusion Dither

Taking the same greyscale image stack that was extracted previously for the Random dither, the Error Diffusion algorithm also looped through the pixels in each row, column and layer in the stack and comparing the original greyscale values to a threshold, outputting 1 if greater and 0 if lesser. However, instead of being compared to a random threshold at every location, the threshold was set at a fixed value of 127, i.e. half the maximum greyscale intensity value. After the comparison of every individual pixel, the error is calculated by taking the output value, multiplying it by 255 to get back to the same scale as the input stack, and subtracting the original value. This error is then split and propagated to the surrounding pixels according to a 3D Error Diffusion Kernel. In this work, the Stucki filter used by Brauer and shown in Figure 3 was used. It is worth noting that this error is only propagated to pixels not yet evaluated by the algorithm.

## Ordered Dither

Initially, four different Ordered dither maps were created by shifting the four quadrants of an 8x8 Bayer 2D Kernel and subsequently moving the first column, top row, or both, to ensure that the pattern spiralled. These four base kernels can be seen in Figure 7. Once the greyscale image stack had been created, the Ordered dithering algorithm looped through the layers. For each layer number, the remainder when divided by four was calculated. This allowed the different kernels to be used for every fourth layer, ensuring that the vertical streak effect was avoided. After the respective kernel was selected, it was replicated to create a threshold map the same size as the input image. At this point the algorithm then looped through each row and column comparing the original to the threshold map, outputting 1 if the original was greater and 0 elsewhere.

$$\begin{aligned}
 M_1 &= \frac{255}{64} \times \begin{bmatrix} 0 & 32 & 8 & 40 & 2 & 34 & 10 & 42 \\ 48 & 16 & 56 & 24 & 50 & 18 & 58 & 26 \\ 12 & 44 & 4 & 36 & 14 & 46 & 6 & 38 \\ 60 & 28 & 52 & 20 & 62 & 30 & 54 & 22 \\ 3 & 35 & 11 & 43 & 1 & 33 & 9 & 41 \\ 51 & 19 & 59 & 27 & 49 & 17 & 57 & 25 \\ 15 & 47 & 7 & 39 & 13 & 45 & 5 & 37 \\ 63 & 31 & 55 & 23 & 61 & 29 & 53 & 21 \end{bmatrix} &
 M_2 &= \frac{255}{64} \times \begin{bmatrix} 40 & 3 & 35 & 11 & 43 & 0 & 32 & 8 \\ 24 & 51 & 19 & 59 & 27 & 48 & 16 & 56 \\ 36 & 15 & 47 & 7 & 39 & 12 & 44 & 4 \\ 20 & 63 & 31 & 55 & 23 & 60 & 28 & 52 \\ 42 & 1 & 33 & 9 & 41 & 2 & 34 & 10 \\ 26 & 49 & 17 & 57 & 25 & 50 & 18 & 58 \\ 38 & 13 & 45 & 5 & 37 & 14 & 46 & 6 \\ 22 & 61 & 29 & 53 & 21 & 62 & 30 & 54 \end{bmatrix} \\
 M_3 &= \frac{255}{64} \times \begin{bmatrix} 62 & 30 & 54 & 22 & 60 & 28 & 52 & 20 \\ 43 & 1 & 33 & 9 & 41 & 3 & 35 & 11 \\ 27 & 49 & 17 & 57 & 25 & 51 & 19 & 59 \\ 39 & 13 & 45 & 5 & 37 & 15 & 47 & 7 \\ 23 & 61 & 29 & 53 & 21 & 63 & 31 & 55 \\ 2 & 34 & 10 & 42 & 0 & 32 & 8 & 40 \\ 50 & 18 & 58 & 26 & 48 & 16 & 56 & 24 \\ 14 & 46 & 6 & 38 & 12 & 44 & 4 & 36 \end{bmatrix} &
 M_4 &= \frac{255}{64} \times \begin{bmatrix} 60 & 28 & 52 & 20 & 63 & 31 & 55 & 23 \\ 2 & 34 & 10 & 42 & 1 & 33 & 9 & 41 \\ 50 & 18 & 58 & 26 & 49 & 17 & 57 & 25 \\ 14 & 46 & 6 & 38 & 13 & 45 & 5 & 37 \\ 62 & 30 & 54 & 22 & 61 & 29 & 53 & 21 \\ 0 & 32 & 8 & 40 & 3 & 35 & 11 & 43 \\ 48 & 16 & 56 & 24 & 51 & 19 & 59 & 27 \\ 12 & 44 & 4 & 36 & 15 & 47 & 7 & 39 \end{bmatrix}
 \end{aligned}$$

Figure 7: The four Dispersed-Dot Ordered Dither kernels, created by shifting the original Bayer 8x8 Kernel.

For all the patterns, both TPMS and dithered, the output was a binarized output image stack the same size as the original. An additional step was implemented to create a second output image stack where all pixels contained within the original CAD geometry were inverted, in order to have two 1-bit depth PNG stacks, the first with 1's in the locations where Material 1 should be deposited and the other with 1's in locations where Material 2 should be deposited. For the STEP printer an accompanying .JSON file with information such as number of layers, material usage and the area of the build plate used for printing was also necessary. For the PolyJet printer, however, the files were required to be recombined into a single image stack with different colours for each of the two "part" materials and a third for the "background", i.e. where neither material should be deposited. The new single

image PNG stacks were then loaded into the VoxelPrint utility and transferred to the printer. Figure 8 shows rigid-rigid, i.e. VW/VB, MJT printed samples for the different interface patterns described in this section.

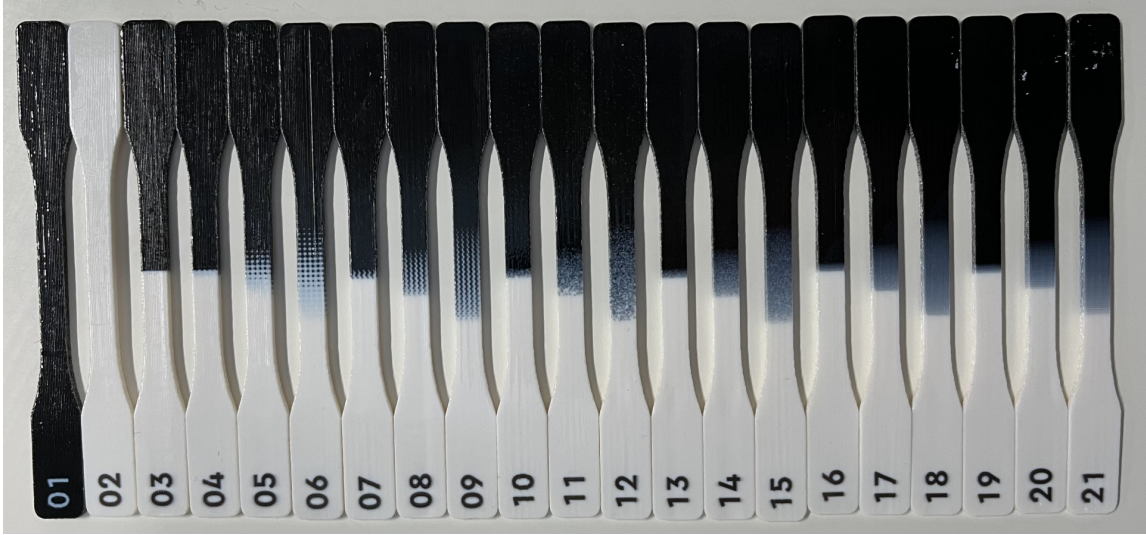


Figure 8: Rigid-Rigid MJT printed samples showing the different interfacial patterns described in Section 2.4.1. The sample numbers correlate to the following patterns/lengths: 1 = VB, 2 = VW, 3 = PI, 4-6 = SP, 7-9 = GY, 10-12 = R2, 13-15 = R3, 16-18 = E3, 19-21 = O3 with interface lengths of 2, 10, and 20 mm for each group respectively.

#### 2.4.2. Interfacial Surface Area Analysis

To record the interfacial surface area, i.e. the area within the part between voxels of Material 1 and Material 2, a separate MATLAB script was used on the STEP PNG stacks to determine the number of times that material changed going between voxels in x, y and z (or row, column and layer). By multiplying these values by the area of one face of the voxel in that direction a total interfacial area can be recorded. Any change between the “part” and the “background” colour is disregarded so that only transitions between the two different part materials themselves increase the count in x, y or z (Algorithm 4 in the supplementary document).

As well as the overall interfacial surface area,  $A_T$ , the area between the two largest regions (i.e. ignoring “floating” voxels / regions that are not connected to the area of the sample held in the clamps) in the direction of tension,  $A_L$ , was also calculated. This was done by removing any pixel not connected to the respective ends from the image stack and running a modified version of the same script which only recorded the area in that direction.

### *2.4.3. Modification to STEP printing process to emulate multi-material printing*

The prototype STEP machine has potential to be equipped with four engines making it possible to print one support material and up to three part materials. However, the machine used in this study only had two EP engines installed and enabled. This therefore limited the potential of printing true multi-material designs since one engine is required to print with support material in order to a) facilitate removal of parts from the build plate, b) print complex 3D designs and c) retain sharp edges within simpler 2.5D parts with a constant cross section in the Z-direction, like the tensile dogbone samples. To mimic MMAM printing with just one part material, a feature of the machine process, whereby the z-height of the build plate can remain at the same height every  $n$  layers, was used. Typically, this feature is used to print several layers with a slight air gap of only a few pixels between part and support material followed by one layer where the z-height stays the same and a thin region of part material is deposited to fill this, thereby improving the surface finish of parts. However, in this case, this technique was used to enable the printing of half a specimen in the odd layers followed by the printing of the second half in the even layers with the z-height changing every other layer. An example of two consecutive layers is shown in Figure 9. Solid samples, where the entire dogbone was printed in either the odd layers (with no material deposited in the even layers) or the even layers (with no material deposited during the odd layers), were also produced in order to make the comparison to samples containing an interface. Previous work in thermoplastic material extrusion has shown that, although the differences in mechanical properties are greater amongst samples made of two different materials, there are still interfacial effects, mirroring those of multi-materials, that can be seen amongst samples where one identical material is used with an interface [42, 43, 44].

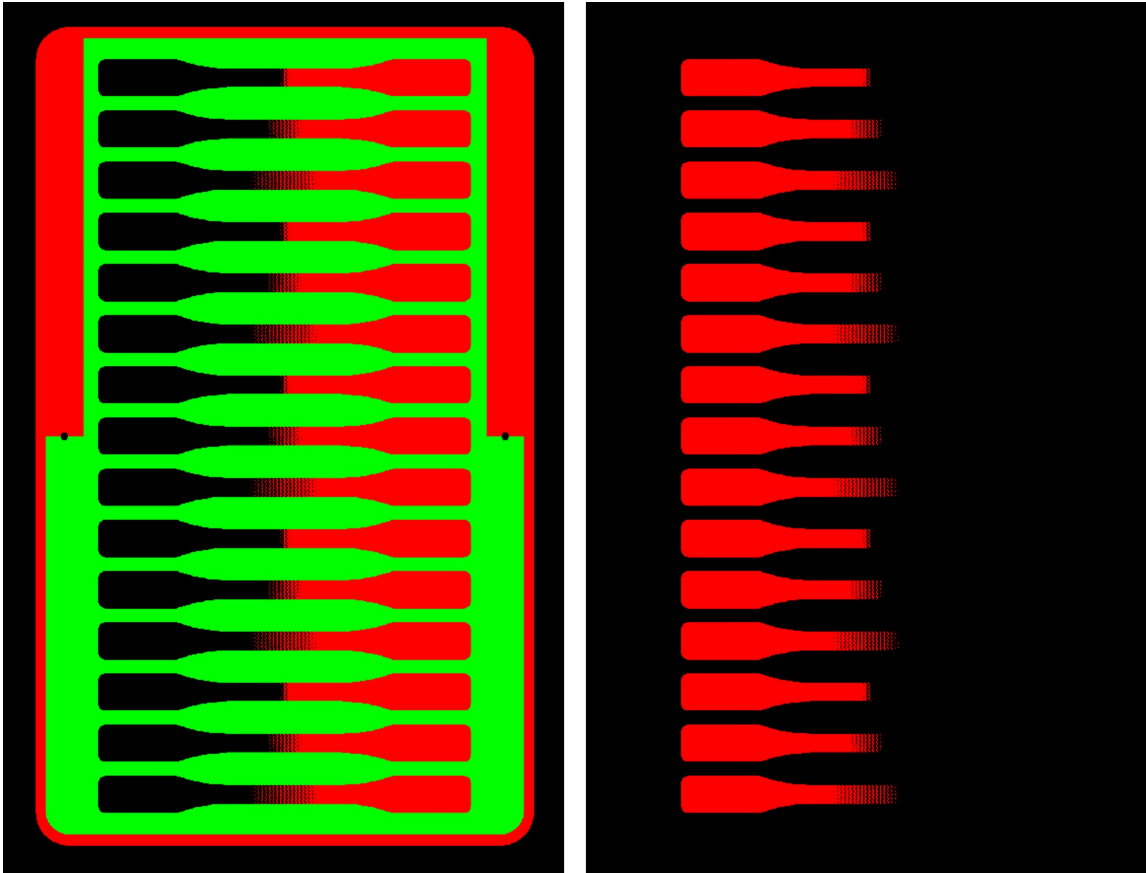


Figure 9: Emulating MMAM with the STEP process. Red = Part material, Green = Support material, Black = Neither material deposited. Left = Odd layer, Right = Even layer.

### 3. Results and Discussion

A calculation of the total surface area between the two materials showed that, for any given length, the TPMS structures (SP and GY) had lower total interfacial area than all the dithered patterns. Specifically, the E3 pattern provided the greatest amount of area between the two materials over the 10 and 20 mm interface lengths, whilst the R3 pattern gave the largest area over the 2 mm gradient (Figure 10 - Top). If, however, only the voxels connected to the largest regions of each of the two materials are considered, most of the dithered patterns interfacial areas were negligible or non-existent (Figure 10 - Bottom). This indicated that these samples contained a centre section, or sections, that were separate from their respective ends. Another way to consider this, is that there existed one or more three dimensional split surfaces in these parts. It is worth noting that Figure 10 shows the data for the STEP samples, values for the PolyJet samples vary in absolute values due to the slight difference in z dimension of the voxel size but follow the same trend for both  $A_T$  and  $A_L$ .

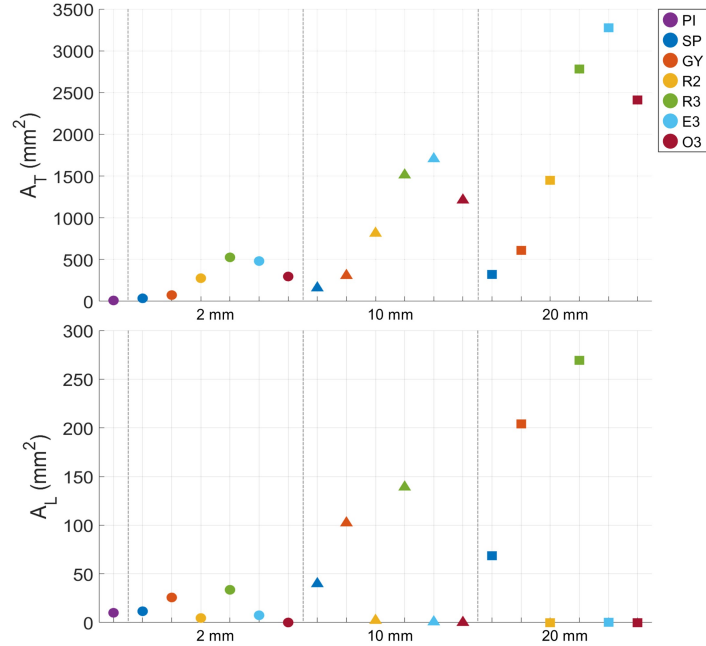


Figure 10: Surface area analysis for STEP parts. Top = Total Surface area,  $A_T$  (mm<sup>2</sup>), Bottom = Surface area in the tensile direction between two largest regions,  $A_L$  (mm<sup>2</sup>). Samples are divided according to the interface length; Circles = 2mm, Triangles = 10mm, Squares = 20mm.

The results of the PolyJet VW and AB samples are shown in Figure 11. The error bars represent  $\pm 1$  standard deviation (s.d.) of the five samples printed per pattern. There was a very large disparity between the results for the Solid VW tensile bars and the rest of the results, hence the results of E and UTS for this data point ( $E = 1383.58 \pm 110.86$  MPa,  $UTS = 19.92 \pm 2.31$  MPa) were left out of the plot to more easily visualise any potential differences between the interface patterns. Amongst previous literature there has been some comments on the failure location in qualitative terms. In particular, Lumpe et al. stated that within MJT parts the more similar the base materials, the more likely they were to fail at the interface rather than in the compliant material. However, failures were also observed directly at the interface for rigid-compliant parts, albeit with a previous version of both compliant material (Tango Black) and printer (Stratasys Connex3 Objet500) [9]. There has, on the other hand, been little attempt previously to quantify these failure locations. In this work, the location of failure from the centre of the sample was recorded, with positive taken as the direction towards the base material with the lower experimentally derived E, in this case AB, and the shading shows the interface region.

Pearson’s correlation coefficient ( $r$ ) was computed to assess linear relationships in the data collected as part of this study. By increasing the length of the interface the overall E value increased, regardless of pattern ( $r(93) = .771$ ,  $p < 0.001$ ). From Figure 11 it can be seen that these parts did not fail in the interface region, indicating that the increased E was not due to a stronger interface region but rather to a reduction in size of the region of the compliant material. In addition, there was also a correlation of a reduction in  $\epsilon_B$  for the increase in gradient length ( $r(93) = -.945$ ,  $p < 0.001$ ), which also supports this hypothesis that it is the change to the compliant region rather than the interface region that was dominating the physical response.

Overall, the UTS results demonstrate smaller differences with respect to the effect of the interfacial pattern than is suggested by some of the previous literature into rigid-compliant PolyJet interfaces. For example, the 3D Random dither sample included by Saldívar et al. [11], or the 3D Error Diffusion dither studied by Brauer [12] both showed a greater increase in UTS when compared to their respective Planar Interface samples than was observed in this work. The SP samples, on the other hand, exhibited a significant reduction in UTS when compared to the PI samples particularly for the 10 and 20 mm interface lengths ( $t(4.535) = 11.585$ ,  $p < 0.001$  and  $t(4.3507) = 11.651$ ,  $p < 0.001$  respectively). Amongst the VW/AB samples, these were also the only pattern and length combinations where all 5 specimens failed within the interface region. This indicated that the SP pattern made the interface weaker than the PI which, when looking at the failure locations (Figure 12), is likely

due to this pattern inducing cracks at locations where there is a split plane of AB between discrete islands of VW. This may also explain why the 2 mm SP sample suffered a smaller reduction in UTS, since the short length of this interfacial pattern does not contain such split planes. As such, this specific SP TPMS pattern should be avoided when designing part interfaces.

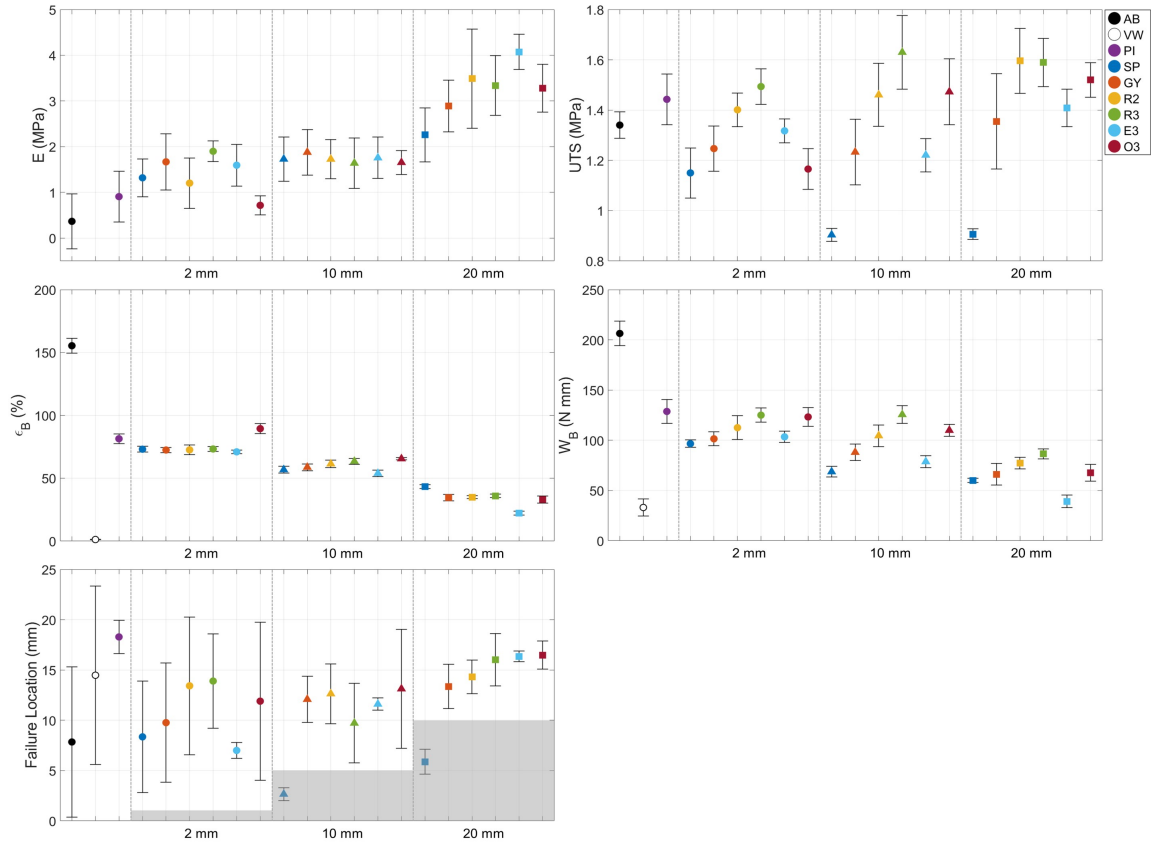


Figure 11: Results of VW/AB PolyJet Samples. Top Left = Young's Modulus (MPa), Top Right = Ultimate Tensile Stress (MPa), Middle Left = Elongation at Break (%), Middle Right = Work at Break (N mm), Bottom Left = Failure Location (mm). Samples are divided according to the interface length; Circles = 2 mm, Triangles = 10 mm, Squares = 20 mm. Shaded region shows the interfacial area.



Figure 12: Failure Locations for the VW/AB SP 20 mm samples.

Results from the rigid-rigid PolyJet (VW and VB) testing are shown in a similar way in Figure 13. From the E data, despite being given the same naming designation from Stratasys, and the data sheet suggesting that they would have very similar properties [38], the VW and VB materials had a 516 MPa (or 33%) difference in Young's Modulus. It is interesting to note that several samples exhibited lower E values than either of the two base materials, suggesting that the interface region had a lower stiffness than either the VW or VB. The SP pattern exhibited the greatest values of E for the longer interface lengths, although the physical reason for this behaviour is unknown and requires further investigation.

The UTS data from this set of experiments showed that there were few differences between all patterns and lengths and that no samples showed significant improvement over the No Interfacial Pattern group; Only the SP/2 mm, SP/10 mm, GY/2 mm, and R2/10 mm combinations had averages higher than the PI samples, but when Welch's T-tests were conducted ( $t(6.498) = 0.755$ ,  $p = .477$ ;  $t(6.541) = 1.921$ ,  $p = .099$ ;  $t(5.215) = 0.043$ ,  $p = .967$ ; and  $t(5.411) = 0.059$ ,  $p = .955$  respectively) these all showed insignificance, i.e.  $p > 0.05$ . Part of the reason for this may be explained by the results of  $\epsilon_B$  for the VB/VW samples. These demonstrated that these rigid PolyJet materials, along with all combinations of interfacial pattern tested in this study, were extremely brittle with a maximum average value of 1.42%, far below the data sheet estimated range of 10 - 25%.

Similarly to the VW/AB samples, the VW/VB samples demonstrated failure locations predominantly outside of the interface region, especially over the shorter interface lengths. This shows that failure is occurring within the more compliant

sections of the samples, in this case VW. For the 20 mm interface length, more of the samples failed near the edge of the interface region although in a less consistent manner than the SP samples the VW/AB experiments; The most consistent failures for rigid-rigid parts was the O3 samples which exhibited a greater s.d. ( $\pm 1.7$  mm) than the rigid-compliant SP parts with 10 and 20 mm interfaces ( $\pm 0.7$  and  $\pm 1.2$  mm, respectively).

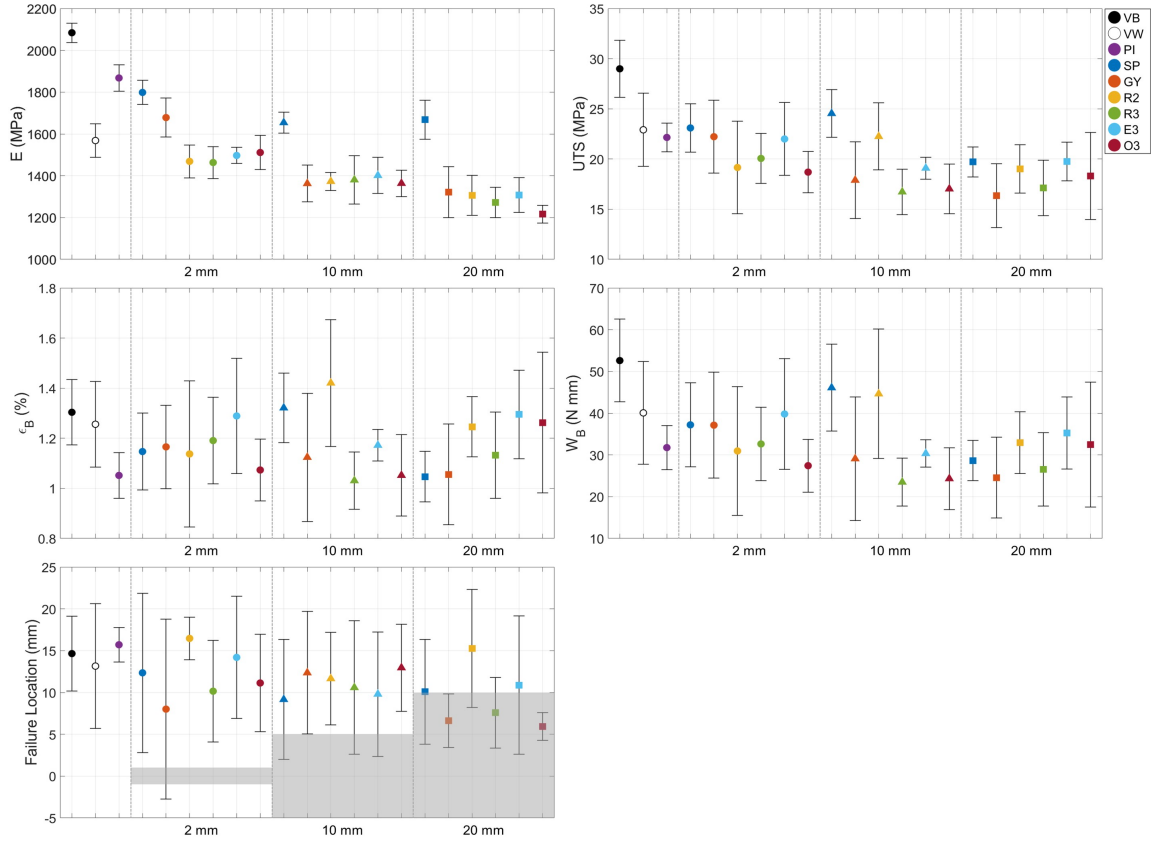


Figure 13: Results of VW/VB PolyJet Samples. Top Left = Young's Modulus (MPa), Top Right = Ultimate Tensile Stress (MPa), Middle Left = Elongation at Break (%), Middle Right = Work at Break (N mm), Bottom Left = Failure Location (mm). Samples are divided according to the interface length; Circles = 2 mm, Triangles = 10 mm, Squares = 20 mm. Shaded region shows the interfacial area.

The results from the STEP process with both halves consisting of the same rigid ABS material but with alternating layers of material deposition are displayed in Figure 14. In general, the values of  $E$  amongst all the patterns as well as the two "solid" samples, i.e. Odd and Even, were similar. This was to be expected given that the parts are comprised entirely of the same material throughout. With regards to the UTS, the dithered samples had slightly lower values than the GY and SP samples,  $t(86.966) = 7.396$ ,  $p < 0.001$ , although the overall relative difference between the minimum and maximum UTS for the STEP interfacial pattern samples (5.8%) was smaller than that of both the VW/AB (44.56%) and VW/VB (33.42%) MJT combinations.

The interface samples from the STEP process did, however, show significantly reduced values in  $\epsilon_B$  compared to the solid samples ( $t(10.154) = 18.308$ ,  $p < 0.001$ ). This indicated the samples with interfaces did not plastically deform and as a result were also significantly less tough, i.e. lower  $W_B$ . There was an additional significant correlation showing an increase in  $W_B$ , for an increase in  $A_L$  ( $r(92) = .809$ ,  $p < .001$ ). This correlation is shown in Figure 15. It can therefore be concluded that the value of  $A_L$  for a three-dimensional dither (or any other interfacial) pattern could be pre-calculated to predict its toughness. Anecdotally, this matches simulation-based results where the toughest interfaces shown by Maurizi et al. are ones where the value of  $A_L$  would be highest (although this value is not calculated as part of their article) [45].

The failure location data for the STEP samples showed that, unlike both sets of MJT samples, the failures almost exclusively occurred within or around the interface region for every pattern. This implies that the interface regions are more prone to failure than the base material and therefore the interfacial geometry is likely to make more of a difference to the overall mechanical properties. An example of this difference in failure location between the STEP and the MJT parts is shown in Figure 16. This figure shows the failure locations of all PI parts, which would be most likely to fail at the interface directly. It can be seen that whilst the STEP sample does indeed fail close to the interface, the MJT failure locations are within the weaker of the two base materials rather than the interface itself.

Some of the differences between the results seen in this work and others in literature may be related to the difference in specimen and an updated generation of MJT printer used compared to most interfacial strength work previously recorded. This work had a sample with only one transition from one material to the other in order to enable longer gradients, and to allow significant regions of the individual materials alongside the interfacial region. Previous studies have predominantly had two interfaces per sample with a transition from one material to the other and

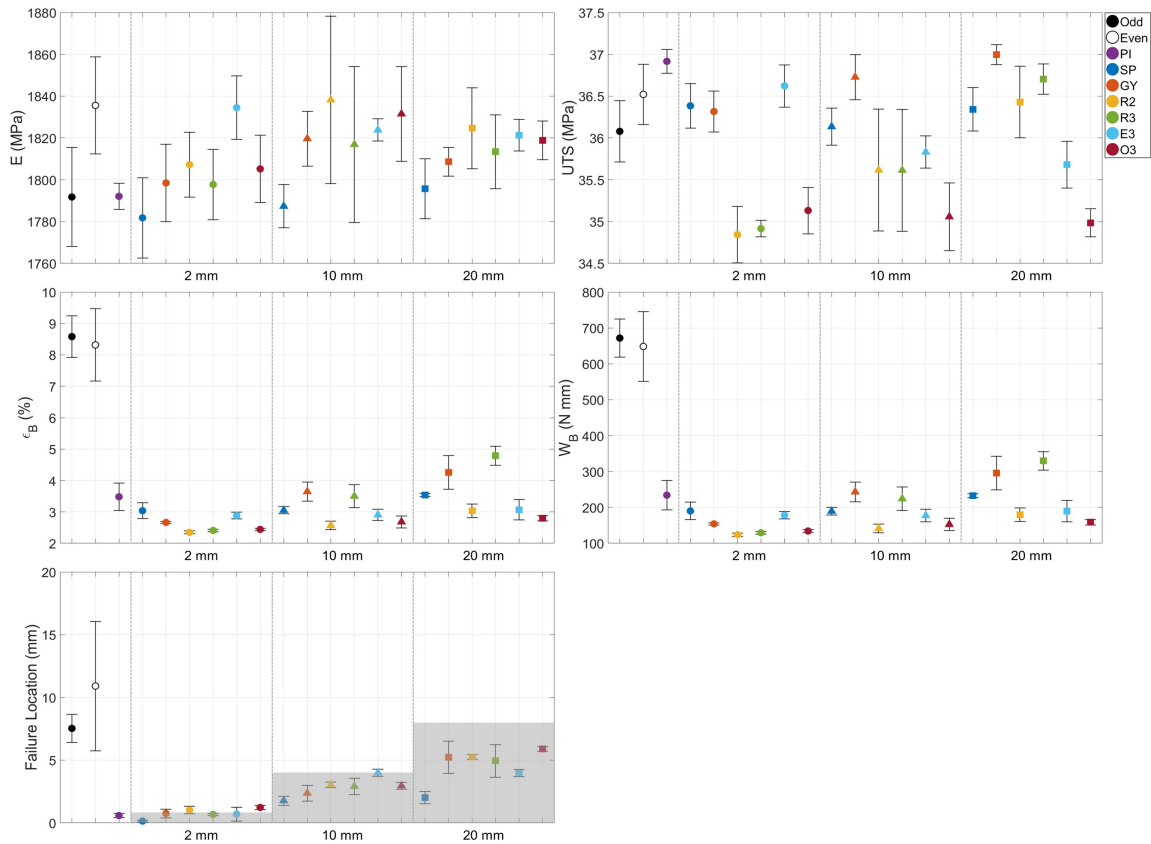


Figure 14: Results of ABS/ABS STEP Samples. Top Left = Young's Modulus (MPa), Top Right = Ultimate Tensile Stress (MPa), Middle Left = Elongation at Break (%), Middle Right = Work at Break (N mm), Bottom Left = Failure Location (mm). Samples are divided according to the interface length; Circles = 2 mm, Triangles = 10 mm, Squares = 20 mm. Shaded region shows the interfacial area.

back again. Similarly, most studies into the strength of interfaces within MJT parts have used older Stratasys machines rather than the J826 machine used in this study. It is fair to assume that there may have been improvements in both the hardware and materials, and that this may be responsible for some improvement in interfacial strength.

Across the results, there are some differences between the STEP and MJT samples. One reason for these differences is likely to be the different adhesion mechanisms between the two base materials in each case. Whereas STEP uses toner-based thermoplastics, the UV curable photopolymers (VW, VB and AB) from the MJT process are able to form strong cross-links between the polymer chains when exposed

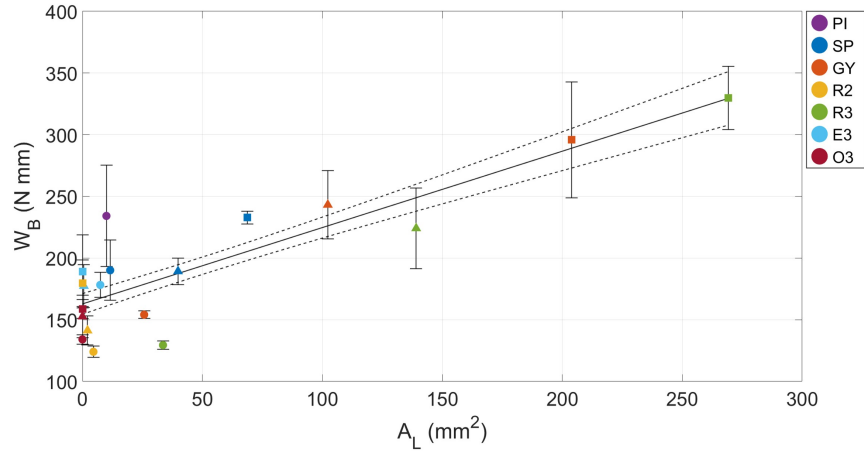


Figure 15: Correlation between the Work at break,  $W_B$ , and the surface area in the direction of tension between the two largest regions,  $A_L$ , for the ABS/ABS STEP samples. The dashed lines show the 95% confidence limits.

to UV light. Whilst both technologies are able to deposit similarly sized voxels of material and both have a consolidating roller which helps join and flatten layers together, this additional cross-linking along with the potential mixing of the two resins after deposition, but before curing, leads to stronger overall bonding between the materials.

The vertical streaking present in the R2 dithering pattern, appeared to have little effect on the mechanical properties across the MJT samples where in all cases except the  $\epsilon_B$  for the 10 mm VW/VB parts, the error bars for R2 and R3 overlapped. The absolute difference in average  $\epsilon_B$  in this case was also only 0.39%. For the STEP parts there were also no differences observed between R2 and R3 in E and UTS. However, in these ABS/ABS parts differences in  $\epsilon_B$  and  $W_B$  emerged that increased the longer the interface lengths. This could be attributed to the R3 dithering pattern allowing connections to form between the largest regions of each material, increasing  $A_L$  (as seen in Figure 10) rather than to vertical streaking or lack thereof, since the O3 and E3 samples without this effect had more comparable values to the R2 than to R3, especially for an interfacial length of 20 mm. It is likely, that the vertical streaks may have more effect in bending rather than tension but this fell outside of the scope of the study.



Figure 16: Failure locations within PI parts of all material combinations. Left = VW/AB, Centre = VW/VB, Right = ABS/ABS.

#### 4. Conclusions and Future Work

This study investigated the effect of material, printer and geometry on the interfacial strength of Functionally Graded Material samples. It described a methodology whereby smooth field driven designs can be discretised into binary outputs allowing production on two different AM processes, both of which can utilise image stacks as an input file format. This is achieved through the extension of long established 2D dithering algorithms into 3D. It also demonstrated a novel AM process, Evolve Additive Solutions' Selective Thermoplastic Electrophotographic Process, and the potential this has to produce MMAM parts from amorphous thermoplastics.

The work has shown that, in general, when parts containing large regions of two different materials are printed using the PolyJet printing technology, the length of the interface has some effect on the mechanical properties analysed since the base materials themselves have different mechanical properties. However, the interface pattern itself has only minimal effects as the parts are more prone to fail in the more compliant of the two materials rather than the interface itself if loaded under tension. This was true for both rigid-rigid and rigid-compliant samples.

On the other hand, STEP parts are likely to fail at the interface due to the thermoplastic base materials having an absence of the cross-linking found in the MJT process. The surface area between connected regions in the direction of tension,  $A_L$ , was shown to have a large impact on the overall toughness of the material. The samples with the largest  $A_L$ , the 3D random dither with 20mm gradient length, demonstrated increases of 37.5% and 40.8% to  $\epsilon_B$  and  $W_B$  respectively, when compared to the sample with no designed interfacial geometry.

There is also a visual difference in the various TPMS and dithering patterns as can be seen from Figure 1 and Figure 8. This may have implications for aesthetic multi-colour prints. Since parts designed for their aesthetic are likely to be subject to minimal loads and the interfacial pattern has been shown to only have a minimal effect on the mechanical properties, a specific dithering pattern can be selected in order to give a distinct appearance, with the error diffusion pattern giving the smoothest gradients overall.

Some limitations of this work are regarding the approach taken using the STEP technology. This AM process is very much in its infancy and as such the single material deposited in two halves to imitate MMAM printing is the best approach currently available on the prototype system. It is expected that there would be more noticeable effects on the mechanical properties if two different materials could be used. However, further developments to both hardware and materials from the manufacturer would be required in order to fully explore the effect of the interfacial structures on true MMAM objects.

Both STEP and PolyJet are processes with relatively fine resolutions for AM where some mixing and consolidation happens in every layer. In addition, the materials used in each combination are chemically similar, even identical in the case of the STEP samples, and, consequently, chemical bonding is occurring at the interface. As such, this may be why the interfaces are in general stronger and less likely to fail than in some other MMAM processes. Future work would, therefore, also include using other MMAM systems that do not contain any form of consolidation roller, can only print at a coarser resolution, and where materials with fundamentally different chemistry can be deposited, e.g. a material extrusion process, in order to produce parts. It would be expected that in cases where there is no chemical bonding at the interface, the three-dimensional dithering approach would have a greater impact since their interfacial strength is entirely dependent on mechanical interference. Additional further work into the strength of three-dimensional dithering patterns in bending along with the effect of process variables within MJT and STEP, such as the temperature distribution within the STEP interface region, on interfacial strength is also recommended.

## References

- [1] A. M. Paterson, R. Bibb, R. I. Campbell, G. Bingham, Comparing additive manufacturing technologies for customised wrist splints, *Rapid Prototyping Journal* 21 (2015) 230–243. doi:10.1108/RPJ-10-2013-0099.
- [2] E. L. Doubrovski, E. Y. Tsai, D. Dikovskiy, J. M. Geraedts, H. Herr, N. Ox-

- man, Voxel-based fabrication through material property mapping: A design method for bitmap printing, *CAD Computer Aided Design* 60 (2015) 3–13. doi:10.1016/j.cad.2014.05.010.
- [3] G. L. Goh, H. Zhang, T. H. Chong, W. Y. Yeong, 3D Printing of Multilayered and Multimaterial Electronics: A Review, *Advanced Electronic Materials* 7 (2021) 2100445. URL: <https://onlinelibrary.wiley.com/doi/10.1002/aelm.202100445>. doi:10.1002/aelm.202100445.
- [4] Y. L. Yap, S. L. Sing, W. Y. Yeong, A review of 3D printing processes and materials for soft robotics, *Rapid Prototyping Journal* 26 (2020) 1345–1361. URL: <https://www.emerald.com/insight/content/doi/10.1108/RPJ-11-2019-0302/full/html>. doi:10.1108/RPJ-11-2019-0302.
- [5] L. Zorzetto, L. Andena, F. Briatico-Vangosa, L. De Noni, J.-M. Thomassin, C. Jérôme, Q. Grossman, A. Mertens, R. Weinkamer, M. Rink, D. Ruffoni, Properties and role of interfaces in multimaterial 3D printed composites, *Scientific Reports* 10 (2020) 22285. doi:10.1038/s41598-020-79230-0.
- [6] I. Q. Vu, L. B. Bass, C. B. Williams, D. A. Dillard, Characterizing the effect of print orientation on interface integrity of multi-material jetting additive manufacturing, *Additive Manufacturing* 22 (2018) 447–461. doi:10.1016/j.addma.2018.05.036.
- [7] J. Mueller, D. Courty, M. Spielhofer, R. Spolenak, K. Shea, Mechanical Properties of Interfaces in Inkjet 3D Printed Single- and Multi-Material Parts, *3D Printing and Additive Manufacturing* 4 (2017) 193–199. URL: <http://www.liebertpub.com/doi/10.1089/3dp.2017.0038>. doi:10.1089/3dp.2017.0038.
- [8] F. Liu, T. Li, X. Jiang, Z. Jia, Z. Xu, L. Wang, The effect of material mixing on interfacial stiffness and strength of multi-material additive manufacturing, *Additive Manufacturing* 36 (2020). doi:10.1016/j.addma.2020.101502.
- [9] T. S. Lumpe, J. Mueller, K. Shea, Tensile properties of multi-material interfaces in 3D printed parts, *Materials and Design* 162 (2019) 1–9. doi:10.1016/j.matdes.2018.11.024.
- [10] E. Salcedo, D. Baek, A. Berndt, J. E. Ryu, Simulation and validation of three dimension functionally graded materials by material jetting, *Additive Manufacturing* 22 (2018) 351–359. doi:10.1016/j.addma.2018.05.027.

- [11] M. C. Saldivar, E. T. W. Shen, E. L. Doubrovski, M. J. Mirzaali, A. A. Zadpoor, Bioinspired rational design of multi-material 3d printed soft-hard interfaces, 2022. [arXiv:2206.13615](https://arxiv.org/abs/2206.13615).
- [12] C. Brauer, Automated Design of Graded Material Transitions for Educational Robotics Applications, Master's thesis, Arizona State University, 2020.
- [13] F. Ulu, R. P. S. Tomar, R. Mohan, Processing and mechanical behavior of rigid and flexible material composite systems formed via voxel digital design in polyjet additive manufacturing, *Rapid Prototyping Journal* 27 (2021) 617–626. doi:10.1108/RPJ-06-2020-0119.
- [14] S. Park, W. Shou, L. Makatura, W. Matusik, K. K. Fu, 3D printing of polymer composites: Materials, processes, and applications, *Matter* 5 (2022) 43–76. URL: <https://linkinghub.elsevier.com/retrieve/pii/S2590238521005178>. doi:10.1016/j.matt.2021.10.018.
- [15] L. Bass, N. A. Meisel, C. B. Williams, Exploring variability of orientation and aging effects in material properties of multi-material jetting parts, *Rapid Prototyping Journal* 22 (2016) 826–834. URL: <https://www.emerald.com/insight/content/doi/10.1108/RPJ-11-2015-0169/full/html>. doi:10.1108/RPJ-11-2015-0169.
- [16] L. N. Bowers, A. C. Ranpara, K. A. Roach, A. K. Knapp, E. D. Arnold, A. B. Stefaniak, M. A. Virji, Comparison of product safety data sheet ingredient lists with skin irritants and sensitizers present in a convenience sample of light-curing resins used in additive manufacturing, *Regulatory Toxicology and Pharmacology* 133 (2022) 105198. URL: <https://linkinghub.elsevier.com/retrieve/pii/S027323002200085X>. doi:10.1016/j.yrtph.2022.105198.
- [17] B. Bayer, An Optimum Method for Two Level Rendition of Continuous Tone Pictures, *IEEE Intl. Conf. Comm.* (1973) 11–15.
- [18] R. W. Floyd, L. Steinberg, An Adaptive Algorithm for Spatial Grayscale, *Proceedings of the Society of Information Display* 17 (1976) 75–77.
- [19] W. Cho, E. M. Sachs, N. M. Patrikalakis, D. E. Troxel, A dithering algorithm for local composition control with three-dimensional printing, *Computer-Aided Design* 35 (2003) 851–867. URL:

<https://linkinghub.elsevier.com/retrieve/pii/S0010448502001227>.  
doi:10.1016/S0010-4485(02)00122-7.

- [20] D. Richards, T. Abram, A. Rennie, Designing Digital Materials with Volumetric Gradients, in: 15th Rapid Design, Prototyping & Manufacturing Conference (RDPM2017), 2017.
- [21] I. F. Ituarte, N. Boddeti, V. Hassani, M. L. Dunn, D. W. Rosen, Design and additive manufacture of functionally graded structures based on digital materials, *Additive Manufacturing* 30 (2019). doi:10.1016/j.addma.2019.100839.
- [22] M. J. Mirzaali, M. E. Edens, A. H. de la Nava, S. Janbaz, P. Vena, E. L. Doubrovski, A. A. Zadpoor, Length-scale dependency of biomimetic hard-soft composites, *Scientific Reports* 8 (2018). doi:10.1038/s41598-018-30012-9.
- [23] D. V. Kaweesa, N. A. Meisel, Quantifying fatigue property changes in material jetted parts due to functionally graded material interface design, *Additive Manufacturing* 21 (2018) 141–149. doi:10.1016/j.addma.2018.03.011.
- [24] D. V. Kaweesa, D. R. Spillane, N. A. Meisel, Investigating the Impact of Functionally Graded Materials on Fatigue Life of Material Jetted Specimens, in: *Proceedings of the 28th Annual International Solid Freeform Fabrication Symposium*, 2017.
- [25] D. V. Kaweesa, N. A. Meisel, Material Property Changes in Custom-Designed Digital Composite Structures Due to Voxel Size, in: *29th Annual International Solid Freeform Fabrication Symposium - An Additive Manufacturing Conference*, 2018, pp. 1499–1510.
- [26] C. Brauer, D. Aukes, J. Brauer, C. Jeffries, *VoxelFuse*, 2020. URL: <https://github.com/cdbrauer/VoxelFuse>.
- [27] Q. Lou, P. Stucki, Fundamentals of 3D halftoning, in: *Lecture Notes in Computer Science*, 1998, pp. 224–239. URL: <http://link.springer.com/10.1007/BFb0053273>. doi:10.1007/BFb0053273.
- [28] R. A. Chudasama, Development of an Acrylonitrile Butadiene Styrene Toner for an Electrophotography Based Additive Manufacturing Process, Ph.D. thesis, DeMonfort University, 2015.
- [29] C. F. Carlson, *Electron photography*, 1940. URL: <https://patents.google.com/patent/US2221776A/en>.

- [30] D. K. Bynum, Automated manufacturing system using thin sections, 1992.
- [31] D. Cormier, J. Taylor, K. Unnanon, P. Kulkarni, H. West, Experiments in layered electro-photographic printing, International Solid Freeform Fabrication Symposium (2000). doi:10.26153/tsw/3047.
- [32] S. Banerjee, D. I. Wimpenny, Laser printing of polymeric materials, International Solid Freeform Fabrication Symposium (2006). doi:10.26153/tsw/7146.
- [33] A. V. Kumar, A. Dutta, Layered Manufacturing by Electrophotographic Printing, Proceedings of the ASME Design Engineering Technical Conference 2 A (2008) 205–211. doi:10.1115/DETC2003/DAC-48724.
- [34] J. Jones, D. Wimpenny, G. Gibbons, C. Sutcliffe, Additive manufacturing by electrophotography: Challenges and successes, International Conference on Digital Printing Technologies (2010). doi:10.2352/ISSN.2169-4451.2010.26.1.art00046\_2.
- [35] A. Rojas Arciniegas, M. Esterman, Exploring surface defects on ep-based 3d-printed structures, Journal of Imaging Science and Technology 58 (2014). doi:10.2352/J.ImagingSci.Technol.2014.58.2.020506.
- [36] M. J. Benning, K. Dalgarno, Proof of concept of a novel combined consolidation and transfer mechanism for electrophotographic 3D printing, Rapid Prototyping Journal 24 (2018) 1040–1048. doi:10.1108/RPJ-04-2018-0111.
- [37] T. Mitsuya, Y. Nagase, Overview and Recent Progress of Electrophotographic Technologies, Journal of Imaging Science and Technology 63 (2019) 40401–1–40401–6. URL: <https://library.imaging.org/jist/articles/63/4/art00002>. doi:10.2352/J.ImagingSci.Technol.2019.63.4.040401.
- [38] Vero product data sheet for J7 and J8 Series, Stratasys, 2021. URL: <https://www.stratasys.com/en/materials/materials-catalog/polyjet-materials/vero/>.
- [39] Agilus30 product data sheet, Stratasys, 2021. URL: <https://www.stratasys.com/en/materials/materials-catalog/polyjet-materials/agilus>
- [40] STEP™ ABS Material Properties Data Sheet, Evolve Additive Solutions, 2023. URL: <https://evolveadditive.com/products/materials/>.

- [41] ISO 527-1:2019, Plastics — Determination of tensile properties — Part 1: General principles, Standard, International Organization for Standardization, Geneva, CH, 2019.
- [42] L. R. Lopes, A. F. Silva, O. S. Carneiro, Multi-material 3D printing: The relevance of materials affinity on the boundary interface performance, *Additive Manufacturing* 23 (2018) 45–52. doi:10.1016/j.addma.2018.06.027.
- [43] S. Kakaraparthi, R. A. Tataru, N. Chen, A new boundary interlock geometry design pattern to strengthen FDM part multi-material interface, *Manufacturing Letters* 33 (2022) 664–669. URL: <https://linkinghub.elsevier.com/retrieve/pii/S2213846322001134>. doi:10.1016/j.mfglet.2022.07.082.
- [44] D. Dairabayeva, A. Perveen, D. Talamona, Investigation on the mechanical performance of mono-material vs multi-material interface geometries using fused filament fabrication, *Rapid Prototyping Journal* 29 (2023) 40–52. URL: <https://www.emerald.com/insight/content/doi/10.1108/RPJ-07-2022-0221/full/html>. doi:10.1108/RPJ-07-2022-0221.
- [45] M. Maurizi, C. Gao, F. Berto, Interlocking mechanism design based on deep-learning methods, *Applications in Engineering Science* 7 (2021) 100056. URL: <https://linkinghub.elsevier.com/retrieve/pii/S2666496821000224>. doi:10.1016/j.apples.2021.100056.

## Acknowledgements

A special thanks to the various colleagues within The LEGO Group for their personal and technical support with sample printing, post-processing and mechanical testing.